Results in Engineering 32 (2026) 111749

Contents lists available at ScienceDirect

Results in Engineering

journal homepage: www.sciencedirect.com/journal/results-in-engineering

Research paper

Bolted–bonded hybrid joints for complex connections beyond lap joints

Jakob Boretzki [a,*], Matthias Albiez [a], Thomas Ummenhofer [a], Justus Mantik [b], Maik Dörre [b], Morten Voß [c], Till Vallée [c], Tobias Evers [c]

[a] KIT Stahl–und Leichtbau, Versuchsanstalt für Stahl, Holz und Steine, Karlsruhe Institute of Technology, Otto-Ammann-Platz 1, Karlsruhe, 76131, Germany
[b] Fraunhofer Institute for Large Structures in Production Engineering IGP, Albert-Einstein-Str. 30, Rostock, 18059, Germany
[c] Fraunhofer Institute for Manufacturing Technology and Advanced Materials IFAM, Wiener Str. 12, Bremen, 28359, Germany

ARTICLE INFO

Keywords:
Hybrid joint
Adhesive bonding
Preloaded bolts
Complex shear
Galvanised steel
Digital image correlation

ABSTRACT

Preloaded bolted-bonded hybrid joints have commonly been characterised using lap-joint specimens loaded predominantly in axial shear. However, many structural connections show complex shear, in which eccentricity and rotation induce additional torsional shear stresses. In this study, a preloaded hybrid joint in complex shear on hot-dip galvanised steel was investigated to extend experimental evidence beyond lap-joint typologies. A slip-resistant bolted reference without adhesive and hybrid configurations using two different epoxy adhesives were examined. Bolt edge distance (e = 15, 25, 35 mm) and outer splice-plate thickness (t_o = 10, 15, 20 mm at e = 15 mm) were varied, and the response was characterised using both machine displacement and DIC-based relative displacement. Across all configurations, a consistent staged response was observed, comprising an initially steep rise, a stiffness transition, attainment of a peak load Fmax, a first pronounced load drop, and a sustained post-drop branch. Hybridisation increased Fmax substantially relative to the friction-only reference, ranging from about +50% at e = 15 mm to about +110% at e = 35 mm for Sikadur 370 (with Scotch-Weld 7240 showing smaller but consistent gains). Edge distance reduced peak resistance for all concepts, but the reduction was substantially stronger for the friction-only reference than for the hybrids, indicating a mitigation of rotation-driven localisation by hybridisation. Overall, adhesive selection was shown to influence not only load capacity but also the kinematic pathway into the post-drop regime, and the dataset was intended to serve as a benchmark for subsequent modelling.

1. Introduction

1.1. Structural adhesive bonding in steel construction

Structural adhesive bonding has long been established in sectors such as automotive and aerospace, yet its uptake in conventional steel construction remains comparatively limited, where welding and bolting continue to dominate for reasons of robustness, inspectability, and codified design practice [1,2]. In the following, the term *joint* refers to the bonded interface assembly (as commonly used in the adhesives literature), whereas *connection* denotes the structural detail transferring forces between steel members. Early structural-steel studies nevertheless demonstrated feasibility for adhesively connected members and already combined bonding with bolting, but the experimental evidence has predominantly relied on comparatively simple coupon-like configurations [3]. Nevertheless, several attributes of adhesive bonding are recognised as directly relevant to civil engineering, including more uniform stress transfer, sealing and corrosion mitigation, vibration damping, and the ability to join thin plates or dissimilar materials without local heat input [4]. –Beyond classical lap-shear geometries, bonded interfaces have also been explored in steel–concrete composite beams, illustrating that structural boundary conditions can introduce markedly different constraint and load-transfer characteristics than standard overlap coupons [5]. At the same time, the transfer of adhesive technology into steel structures is constrained by steel-specific challenges, notably sensitivity to surface condition, difficulties in quality assurance over large bonded areas, and long-term durability under variable environments [6]. –Sullivan and Peterman [7] noted that steel-to-steel adhesive connections are still evaluated predominantly using lap-joint standards, such that the reported strengths are strongly influenced by coupon geometry and boundary conditions and cannot be assumed to transfer to structurally realistic details governed by restraint, contact interaction and multiaxial stress states. This directly underpins the focus of the present paper on a non-classical joint geometry and its experimentally observed failure mechanisms, and situates the study within the broader need for structurally representative validation of adhesive steel connections.

* Corresponding author.
E-mail address: jakob.boretzki@kit.edu (J. Boretzki).

https://doi.org/10.1016/j.rineng.2026.111749
Received 23 March 2026; Received in revised form 21 May 2026; Accepted 26 June 2026
Available online 29 June 2026

A persistent concern is the behaviour of bonded joints on zinc-coated (galvanised) steel. Early automotive-oriented studies on bonding to such substrates report technically attractive lap-shear strength levels [8], while also demonstrating a pronounced dependence on environmental exposure, thereby identifying durability (rather than initial strength alone) as a governing issue for coated interfaces [8]. Complementary investigations attribute failure localisation and bond failure modes to surface morphology and oxide-layer chemistry, and they discuss bondline corrosion phenomena [9]. In parallel, the coatings literature argues that adhesion performance on hot-dip galvanised steels is controlled by surface chemistry and morphological features, with review-level synthesis highlighting how surface treatments and interfacial chemistry govern both adhesion and durability [10].

Consistent with these findings, the performance of bonded joints in structural steel is often governed less by bulk adhesive behaviour than by the weakest link in the interphase, which includes oxide layers, contamination, and industrial or metallic coatings that are not originally specified for bonding [1]. In construction practice, zinc coatings remain common for corrosion protection, but they also introduce distinct chemical and morphological boundary conditions that affect adhesion and its retention under environmental exposure [9,10]. Practical guidance therefore emphasises the pivotal role of surface preparation (e.g. blasting or controlled cleaning) and the need for test methods that reflect the intended substrate state [1,11], particularly when bonding has to be performed on coated steel surfaces [6]. From a mechanical perspective, adhesively bonded joints are characterised by strongly non-uniform stress fields, in which peak shear and peel stresses arise near overlap ends and geometric discontinuities, thereby coupling joint performance to geometry and load path rather than to a single intrinsic strength value [12,13]. In hybrid steel connections, these field effects may be further modified by restraint, contact interaction and evolving load partitioning, which motivates connection-level modelling approaches that resolve the bondline stress state explicitly [14,15]. Accordingly, evidence derived from classical lap-shear characterisation does not necessarily transfer to connection details with pronounced eccentricities, constrained rotation, or local compliance features, which motivates targeted research on complex bonded geometries representative of structural practice [7].

1.2. Hybrid connections

To mitigate perceived risk and overcome functional limitations of purely bonded joints, hybrid connections combine adhesive bonding with mechanical fasteners [16]. In these concepts, the adhesive layer does not only contribute to ultimate resistance; it also increases initial stiffness, reduces local deformation demands, and provides sealing and corrosion protection [17]. The mechanical component, by contrast, supplies redundancy and a residual load path in the event of bond degradation [14,16]. In steel structures, redundancy is particularly attractive because inspection and acceptance requirements remain conservative, and because retrofitting often involves existing surfaces of uncertain condition [1,18].

Hybridisation is also motivated by load-transfer mechanics. When a fastener is present, the adhesive can carry load from the onset, which delays bolt bearing and reduces the slip demand required to mobilise resistance in clearance holes [4]. Conversely, the fastener restrains opening displacements and redistributes load once local bond failure initiates, which is beneficial under variable loading and in the presence of unavoidable manufacturing scatter [18,19]. This focus on redundancy aligns with observations that zinc-coated interfaces may exhibit environmentally sensitive failure loci and corrosion-related degradation modes [8], for which an alternative load path remains advantageous even when initial lap-shear performance appears satisfactory [9]. –Recent analytical developments further indicate that local compliance effects such as bolt-hole deformation and evolving contact can govern the global response of hybrid connections, reinforcing that connection behaviour in structural details may deviate substantially from idealised overlap-coupon assumptions [20].

1.3. Selection rationale of bonded, bolted and hybrid joints

The selection of bonded, bolted and hybrid joints is governed not only by ultimate resistance, but also by load-transfer characteristics, inspection requirements, damage tolerance, and service conditions. Bonded joints provide distributed load transfer, avoid local heat input, and reduce stress concentrations associated with discrete fasteners, but remain sensitive to surface preparation, adhesive selection, durability, and inspection limitations. Recent work on bonded composite patch repairs has shown that adhesive stiffness and strength can affect repair efficiency and crack-tip shielding [21]. Fracture-toughness investigations on adhesively bonded CFRP joints further demonstrated that surface treatment strongly influences damage evolution and joint resistance, highlighting the practical relevance of interface preparation [22].

Bolted joints, by contrast, provide an established, inspectable, and mechanically redundant load path, but introduce local stress concentrations, hole-related weakening, and bearing or slip mechanisms. Hybrid bonded–bolted joints combine the distributed transfer of the adhesive layer with the residual mechanical load path of the fastener. They are therefore selected when both efficient load distribution and damage-tolerant residual resistance are required. Recent aluminium–FRP repair studies similarly showed that mechanical fasteners can preserve a secondary load path after local adhesive damage and improve retained capacity after pre-damage and hydrothermal ageing [23]. Although this application differs from the present galvanised-steel joints, it supports the broader relevance of hybridisation as a strategy for combining adhesive transfer with mechanical redundancy.

1.4. Pretensioned bonded–bolted hybrid connections

Within the broader class of hybrid connections, configurations that combine adhesive bonding with pre-tensioned high-strength bolts receive particular attention, because bolt pretension introduces compressive normal stresses that modify both frictional slip resistance and adhesive failure conditions [4,17]. In the following, bolt pretension refers to the tensile force introduced into the bolt during tightening, which generates compressive contact stresses at the faying surfaces. Two complementary interpretations are discussed in the recent literature. In one view, the hybrid connection is treated as a friction-grip bolted connection in which the cured adhesive augments the frictional interface, effectively adding a cohesive contribution to friction [18,24]. In the other, it is described as an adhesively bonded connection for which pretensioning suppresses peel stresses at overlap ends, delays crack initiation, and increases effective shear capacity [15,17].

Large-scale double-lap experiments provide quantitative evidence of pronounced stiffness and capacity gains achievable through pretensioning [4]. In the test programme of Denkert et al. [4], hybrid connections on galvanised and coated S355 substrates exhibit a rapid load increase to approximately 350 kN within the first 0.025 mm of relative displacement, i.e. before appreciable slip develops. The same study shows that slip resistance in purely pre-tensioned bolted connections depends strongly on surface condition: mean values are reported at about 214 kN for galvanised surfaces, but only around 75 kN for coated counterparts [4]. This contrast illustrates why adhesive hybridisation is attractive when coatings limit friction coefficients. Service behaviour also does not scale linearly with pretension level; once a threshold of roughly half the scheduled bolt pretension force ($0.5\,F_{p,C}$) is exceeded, the average service load changes little with further increases in pretension [4]. In addition, hybrid configurations exhibit reduced scatter, which is relevant to characteristic resistance definitions [15].

Beyond plate lap joints, hybrid technologies are also explored for hollow-section applications, where adhesive layers are integrated into

node or sleeve-type details to reduce stress concentrations and fabrication effort [2]. Numerical investigations on tubular jacket-type connections suggest that global deformation is only weakly affected by adhesive stiffness, whereas local adhesive stresses increase markedly with increasing stiffness, underscoring the need for mechanically consistent modelling at the interface level [2]. These findings are consistent with surface-focused work on zinc-coated steel, in which substrate morphology and chemistry are implicated in interfacial failure localisation and degradation phenomena [9]. They indicate that both local interface state and global constraint conditions must be represented with care, as also emphasised in coatings-oriented synthesis [10]. –In this context, the emergence of models that explicitly represent local deformation and contact effects in hybrid connections highlights that geometrical complexity is not merely a boundary condition but can become a governing mechanism, thereby motivating systematic experimental benchmarks beyond classical lap-shear configurations [7,20].

1.5. Effects of adhesive behaviour, geometry, bolt pretension, failure modes, and modelling

The mechanical role of the adhesive is governed not only by elastic modulus and cohesive strength, but also by sensitivity to multiaxial stress states. In pretensioned hybrid connections, the adhesive layer is subjected to coupled shear and normal stresses: compression arises from bolt clamping, whereas tension develops locally near overlap ends or along eccentric load paths [15]. Off-axis and Arcan-type testing is employed to characterise such interactions [25], and it is further recognised that different shear test methods yield systematically different apparent strengths because constraint conditions and stress gradients differ between setups [11]. For different adhesives, combined-stress test data indicate that shear resistance increases under compressive normal stress [26]; under tensile normal stress, a cut-off behaviour is reported, beyond which little or no shear capacity is mobilised once a critical tensile level is exceeded [26]. These observations motivate mixed-mode failure envelopes (e.g. Mohr–Coulomb-type or related criteria) instead of single-parameter strength descriptions [17].

Joint geometry is similarly decisive. For bonded–bolted hybrid connections in steel construction, a systematic parameter study shows that increasing joint width increases failure load approximately linearly [27]. Increasing overlap length, however, provides diminishing returns and may reduce average shear strength as overlap increases, consistent with stronger stress concentrations and size effects [27]. Longer overlaps also exhibit multi-peak load–displacement responses, with peaks occurring at millimetre-scale displacements, which suggests progressive damage and redistribution rather than abrupt failure [27]. Within the investigated ranges, edge distance shows little influence, supporting the view that governing mechanisms are controlled by the overlap stress field rather than by simple net-section effects [27]. Related experimental–numerical investigations identify distinct failure patterns, including cohesive failure within the adhesive and interfacial failure influenced by coating layers [19], as well as mixed or “special cohesive” modes that reflect complex interphase damage under combined stresses [1]. Earlier work on zinc-coated steel likewise indicates that failure loci can be governed by substrate-side chemistry and morphology [9], and that environmentally assisted degradation may manifest as bondline corrosion even when bulk adhesive behaviour appears adequate [8].

Bolt pretension affects these mechanisms through multiple channels. First, pretension increases interface compression and thus frictional resistance, which changes the partitioning between adhesive shear transfer and frictional load transfer [18]. Second, the compressive field reduces local peel stresses and delays crack initiation near overlap ends [15]. Third, pretension influences manufacturing outcomes: adhesive squeeze-out and cure shrinkage can alter effective bondline thickness and clamp force retention, which requires careful experimental control and measurement [4]. In this context, the established emphasis on zinc-coating surface chemistry and morphology for adhesion performance remains directly relevant [10], because pretension increases local contact pressures and may shift damage evolution towards near-surface phenomena [9].

For modelling and design, these findings necessitate approaches that couple local interface mechanics with global joint behaviour, because stress and damage evolve at the bondline scale while resistance is assessed at the joint scale [28]. Probabilistic finite-element modelling is proposed for pretensioned hybrid connections, where multiaxial interaction data from off-axis characterisation are translated into failure criteria and embedded into weakest-link frameworks with size effects (e.g. Weibull-type formulations) [15,28,29]. Using such workflows, average prediction errors on the order of 10 % are reported across multiple combinations of surface condition, adhesive, and pretension level [15,29]. It is also emphasised that maxima of normal and shear stresses do not necessarily co-locate within the bondline, such that identifying governing “critical combinations” requires explicit field evaluation rather than pointwise checks [15]. This assessment aligns with review-level conclusions that incomplete parameter isolation, limited replicate numbers, and manufacturing variability continue to obscure the relative importance of overlap length, bolt positioning, adhesive choice, and pretension level in many published campaigns [18,28].

1.6. Motivation and scope of the present work

Despite the substantial progress outlined above, a central limitation remains that all of the available evidence is derived from single- and double-lap specimens loaded primarily in uniaxial shear. Yet, typical connection details in steel construction often involve complex loading. This applies, for example, to flanged sheet-metal joints or spliced web joints for I-beams. The performance of these details cannot be emulated by lap specimens under uniaxial shear loading. Thus, the current state of knowledge regarding hybrid joints does not take into account a decisive portion of joint types frequently used in steel construction.

The present work therefore investigates, for the first time, hybrid joints under complex shear. This extends the experimental basis towards loading scenarios in which combined in-plane actions and constrained deformation produce non-trivial normal–shear stress interaction within the bonded interface.

Accordingly, the quasi-static load-bearing behaviour of pretensioned bonded–bolted hybrid connections under complex shear loading is investigated experimentally, and the resulting dataset, including load–displacement response, stiffness evolution, and observed failure manifestations, is established as a reproducible benchmark. In order to investigate a large test matrix with more parameters, a simplified joint geometry was initially developed by means of numerical studies. This simplified geometry shows a stress distribution in the adhesive layer comparable to that present in a spliced web joint and thus allows the insights gained from the simplified geometry to be conferred to the complex geometry as well.

The experimental investigation is intended to enable traceable validation and calibration of mechanistic models. Numerical modelling and strength prediction are therefore deferred to a subsequent paper, in which the experimental results reported herein are used explicitly as the primary reference for model assessment and predictive performance.

2. Materials and methods

2.1. Adhesives

Two cold-curing, two-part epoxy adhesives were used for the hybrid specimens: Sikadur 370 (Sika AG, Baar, Switzerland; hereafter SD370) and Scotch-Weld 7240 (3M, St. Paul, MN, USA; henceforth abbreviated SW7240). Reference material data were taken from a comprehensive mechanical and thermo-mechanical characterisation reported for these products in a closely comparable context of pretensioned hybrid joints [30].

Table 1
Reference properties of the epoxy adhesives used (reported in [4]).

Property	Sikadur 370 (SD370)	Scotch-Weld 7240 (SW7240)
Tensile strength (bulk), f_t [MPa]	25.3 ± 0.7	25.9 ± 1.0
Elongation at break (bulk), ε_b [%]	1.2 ± 0.3	1.9 ± 0.3
Young's modulus (bulk tensile), E [MPa]	3582 ± 347	1832 ± 54
Poisson's ratio (bulk), ν [-]	0.31 ± 0.09	0.40 ± 0.02
Lap-shear strength on galvanised steel, τ_{ls} [MPa]	25.1 ± 0.6	29.3 ± 1.5
Glass transition temperature, T_g [°C]	73	75

In that characterisation, lap-shear strengths were determined on steel substrates in accordance with EN DIN 1465 (reported for both blasted galvanized surfaces). Glass transition temperatures were obtained by dynamic mechanical analysis (DMA) following EN 6721-11. Bulk tensile properties (Young's modulus, Poisson's ratio, tensile strength, and elongation at break) were measured on cured dog-bone specimens according to EN DIN 527. The resulting dataset (Table 1) was used as reference input for interpreting differences between SD370 and SW7240 in the present experimental programme.

In a closely comparable hybrid-joint configuration on blasted S355MC steel substrates, a pronounced spatial variation of the bondline thickness was reported as a consequence of squeeze flow during bolt tightening [31]: for SW7240, thicknesses were reported to range from about 20 μm near the borehole to about 160 μm at the outer corners (mean about 85–90 μm), whereas for S370 markedly larger values were reported (about 200–320 μm, mean about 256–260 μm) [31]. For hybrid joints on galvanised steel, the adhesive thickness at the overlap end was reported to have been about 160 μm for SW7240 and about 320 μm for S370 [29]. Off-axis tests were further conducted on galvanised steel to investigate combined normal and shear loading for both adhesives [29]; for S370 and SW7240, bilinear envelopes in the (σ, τ) plane were reported to describe the data well ($r^2 \approx 0.9$), while an almost linear relationship was reported in the (σ_P, σ_1) representation ($r^2 \approx 1.0$), where σ_P denoted the hydrostatic pressure and σ_1 the maximum principal stress [29]. However, scatter was reported to have been twofold larger for SW7240 than for S370, indicating a more consistent response for S370 under combined loading; additional discussion thereon will follow in Section 4.5.

2.2. Steel and bolts

2.2.1. Steel adherents

The inner and outer adherents were manufactured from structural steel grade S355J2 (material number 1.0577) supplied as quality flat steel in accordance with EN 10058. All adherents were hot-dip galvanised in accordance with ISO 1461 by immersion in molten zinc at approximately $T \approx 450\,°C$. During galvanisation, a metallurgically bonded zinc coating was formed through diffusion reactions between iron and zinc, resulting in a layered structure comprising Fe–Zn intermetallic phases (Γ, δ, ζ) adjacent to the steel substrate and an outer η-phase consisting predominantly of metallic zinc after cooling. Following galvanisation, a passive surface film was formed on the zinc surface.

The hot-dip galvanised steel substrates used in the present study exhibited a zinc coating thickness of 106.7 ± 10.5 μm, as determined by magneto-inductive measurements in accordance with DIN EN ISO 2178. The coating thickness thus lies within the typical range for batch hot-dip galvanised structural steel and defines the substrate condition for all bonded and hybrid specimens considered.

Prior to assembly, the galvanised faying surfaces were degreased by wipe-cleaning using commercial isopropanol in order to remove contaminants and ensure repeatable bonding conditions. Isopropanol was selected because previous investigations had shown sufficient bond strengths for this cleaning procedure. More aggressive solvents, such as butanone, were not used because the personal protective equipment required for their application would be unsuitable for a building-construction context.

2.2.2. Bolting system and measures to suppress unintended bearing

Preloadable high-strength bolting assemblies were employed, consisting of galvanised M12 HV bolt sets in accordance with EN 14399-4, strength class 10.9. In order to prevent an unintended shear–bearing contribution associated with an adhesive-filled annulus in the bolt hole, the specimen fabrication was adapted. In preliminary trials, adhesive extrusion into the clearance between bolt shank and hole wall had been observed, which could have promoted early bolt-to-hole contact and thereby introduced a bearing-type load transfer mechanism. For the preloaded hybrid series, the bolt-hole diameter was therefore increased from 13 mm to 16 mm, resulting in a clearance of 2 mm between bolt shank and hole wall, to mitigate adhesive filling of the annular gap. Furthermore, a dedicated manufacturing fixture (described below in Section 2.3.3 and Fig. 3) was developed. This fixture ensures correct alignment of the adherents prior to bolt installation, and allows residual adhesive to be removed from the bolt holes prior to bolt installation. The bolts were centred in the holes using dedicated inserts (details described below in Section 2.3.3) so that form fit between bolt and hole wall was avoided at the beginning of testing.

2.2.3. Bolt installation and preloading

After insertion of the bolts and placement of washers and nuts, the assemblies were preloaded using the combined torque method in accordance with EN 1090-2. The tightening procedure consisted of an initial tightening torque of 67 Nm, followed by an additional rotation of 90°. This procedure corresponds to a minimum preload of $F_{p,C} = 59$ kN. The described sequence (cleaning, adhesive application where applicable, removal of adhesive residues from bolt holes, and subsequent installation and preloading) was selected to achieve a defined preload while limiting fabrication-induced artefacts in the vicinity of the bolt holes; the torque–pretension relationship and the tightening procedure had been calibrated in an almost identical setting in a previous study using strain gauges embedded in the bolts [30]. For epoxy-based hybrid joints, moderate deviations from the nominal pretension were not expected to be decisive for the load-bearing capacity, as only a weak sensitivity to pretension relative to experimental scatter was reported in a dedicated study [32].

2.3. Specimen concept, geometry, and parameters

2.3.1. Derivation of simplified test specimen

A parameter study on full structural details with complex shear loading, as depicted in Fig. 1a, would have been disproportionately demanding in terms of fabrication and testing effort. Therefore, the investigated configuration was derived from a representative splice-joint detail by means of a numerical transition to a reduced, eccentrically loaded three-plate specimen. The underlying motivation and the derivation route are summarised in Fig. 1: the complex joint was first transferred into a numerical model (Fig. 1a), and a simplified specimen geometry was then selected such that a comparable stress state was introduced into the bondline under global loading (Fig. 1b).

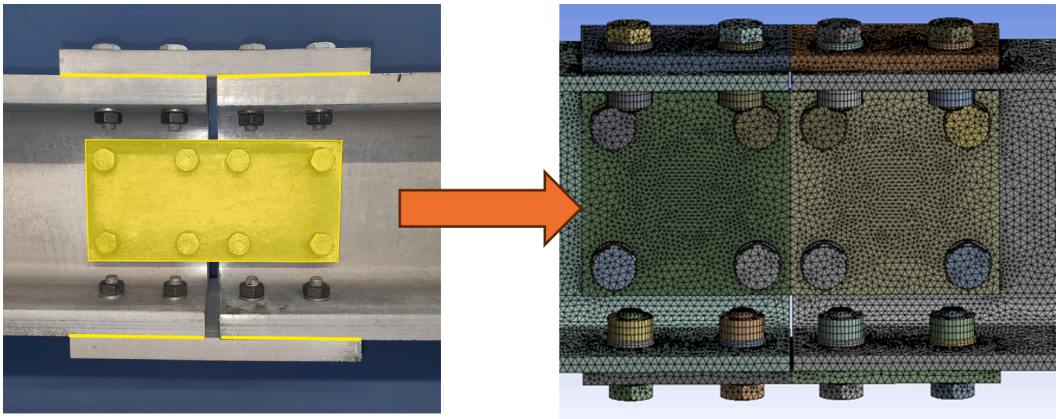

(a) Transition of a splice joint with pre-tensioned hybrid (bonded–bolted) connections into a numerical model.

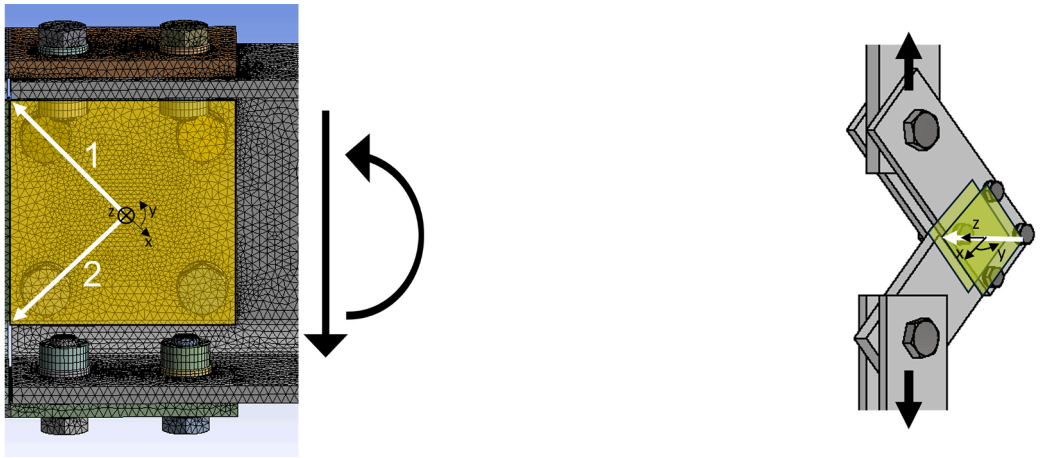

(b) Spliced web joint and corresponding simplified specimen geometry selected for the parameter study.

Fig. 1. Derivation of the simplified specimen geometry for representing complex shear-loaded hybrid joint behaviour in a controlled laboratory configuration.

2.3.2. *Specimen dimensions and variants*

The simplified specimen consisted of two outer splice plates and one inner splice plate. The outer splice plates were manufactured with nominal thicknesses of $t_o = 10\,\text{mm}$, $15\,\text{mm}$, and $20\,\text{mm}$, while their in-plane geometry was otherwise kept identical. Additionally, the inner splice plates were varied in the bolt-hole layout in order to realise different bolt edge distances. The dimensions of the inner-plate variants and the corresponding hole patterns are shown in Fig. 2.

2.3.3. *Manufacturing fixture and assembly sequence*

A dedicated manufacturing fixture was utilised to ensure repeatable alignment of the adherents and to facilitate bolt installation for the different edge-distance configurations. The fixture concept and the placement of adherents are illustrated in Fig. 3. In order to maintain bolt centring in oversized holes and to ensure consistent washer seating across edge-distance variants, slotted holes were used in combination with 3D-printed inserts made of polylactide (Fig. 4). The different insert arrangements were selected such that a clearance of $24\,\text{mm}$ was maintained, corresponding to the washer diameter and the bolt-head width across corners. This ensured concentric alignment of the bolts within the oversized holes for all edge-distance configurations.

Prior to assembly, the bonding surfaces were wipe-degreased using isopropanol. Where applicable, the adhesive was applied to the mating surfaces, and the plates were positioned in the fixture (Fig. 5). A preliminary compression step was conducted using screw clamps to expel excess adhesive from the bondline while bolts were not yet installed. Adhesive residues pressed into the bolt holes were subsequently removed, after which the bolts were inserted, washers and nuts were installed, and final tightening was performed according to the combined torque method in accordance with EN 1090-2.

2.3.4. *Test series and naming scheme*

A total of thirteen test series was defined, with three nominally identical replicates per series. The experimental matrix is summarised in Table 2. The parameter space was spanned by (i) the connection concept / adhesive system (preloaded slip-resistant bolted reference versus preloaded hybrid joint with one of two epoxy adhesives), (ii) the bolt edge distance e ($15\,\text{mm}$, $25\,\text{mm}$, $35\,\text{mm}$), and (iii) the outer splice plate thickness t_o ($10\,\text{mm}$, $15\,\text{mm}$, $20\,\text{mm}$). The preloaded bolted reference configuration was tested for $t_o = 10\,\text{mm}$ across all investigated edge distances, whereas the thickness variation for $t_o = 15\,\text{mm}$ and $20\,\text{mm}$ was considered for hybrid joints at $e = 15\,\text{mm}$.

Variations in joint-component thickness were not examined for the friction-only reference joints, as component thickness is not explicitly considered in the standard design of friction joints and was therefore assumed to be of negligible influence for this configuration. For the hybrid joints, however, component thickness was included as a parameter because it was expected to affect the distribution of compressive stresses in the adhesive layer and thereby influence the hybrid load-transfer mechanism.

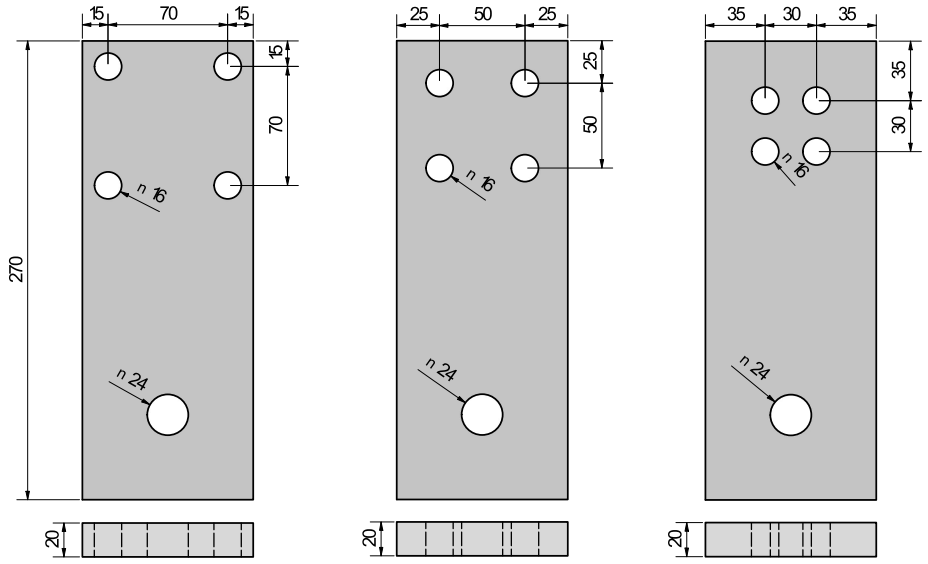

Fig. 2. Inner splice plate variants used to realise different bolt-hole patterns and edge distances, all dimensions in mm.

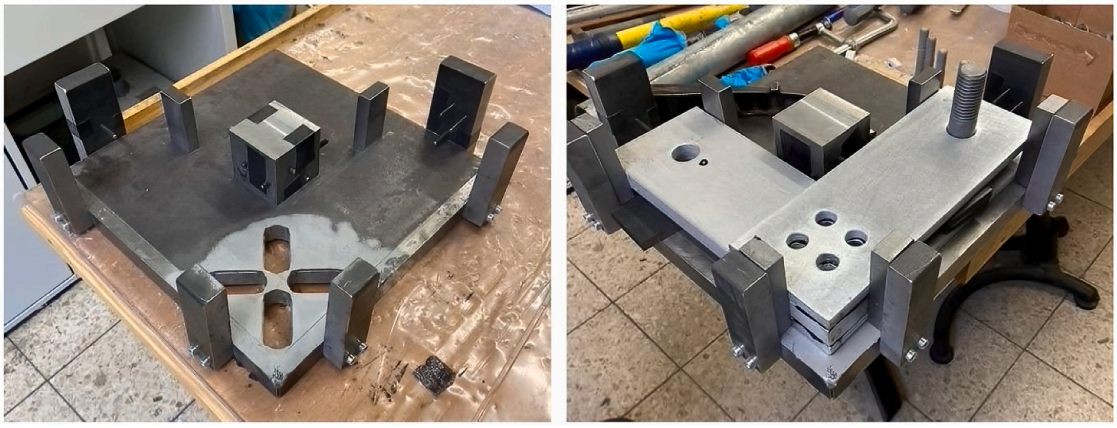

Fig. 3. Manufacturing fixture shown without and with inserted adherents.

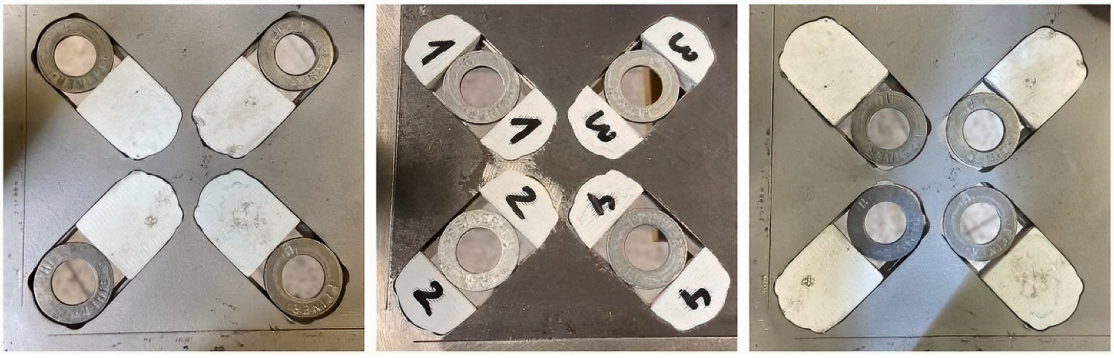

Fig. 4. Slotted holes with 3D-printed inserts and inserted washers used for the various edge distances.

Table 2
Overview of the test series and their denomination. Each series comprised three specimens.

Geometrical parameters		Connection type (and adhesive)		
t_o (outer splice plate)	e (bolt edge distance)	GV reference	Hybrid SD370	Hybrid SW7240
10 mm (S)	15 mm	GV-S-15	SD-S-15	SW-S-15
10 mm (S)	25 mm	GV-S-25	SD-S-25	SW-S-25
10 mm (S)	35 mm	GV-S-35	SD-S-35	SW-S-35
15 mm (M)	15 mm	–	SD-M-15	SW-M-15
20 mm (L)	15 mm	–	SD-L-15	SW-L-15

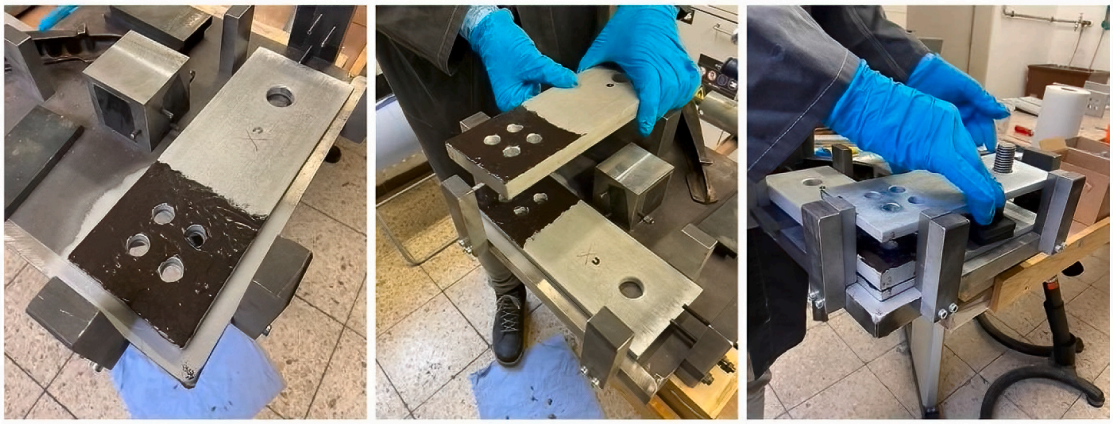

Fig. 5. Insertion of adherents with applied adhesive into the manufacturing fixture.

The naming convention was defined as follows. The first two letters identified the connection type and, where applicable, the adhesive: `GV` denoted the preloaded slip-resistant bolted reference series without adhesive; `SD` denoted the preloaded hybrid series manufactured with SD370; and `SW` denoted the preloaded hybrid series manufactured with SW7240. The outer-plate thickness was encoded by `S` (10 mm), `M` (15 mm), and `L` (20 mm). The bolt edge distance was appended as an integer without unit (15, 25, or 35), and the final identifier corresponded to the specimen number within the series. Consequently, `SD-S-25-3` denoted a hybrid specimen produced with SD370, with $t_o = 10$ mm and $e = 25$ mm, representing the third specimen of that series.

2.4. Experimental procedure

2.4.1. Mechanical testing and specimen fixation

Quasi-static mechanical tests were performed on a hydraulically operated universal testing machine with a nominal capacity of 250 kN. The tests were conducted under displacement control. Unless stated otherwise, a crosshead (machine displacement) rate of 0.5 mm/min was applied. A representative specimen installed and ready for testing is shown in Fig. 6; the blue illumination was used for the digital image correlation (DIC) measurements.

2.4.2. Measurements and monitoring

During testing, the machine force and the machine displacement were recorded continuously. In addition, optical measurements were carried out on one side of the joint region using a DIC system (LIMESS, LIMESS Messtechnik und Software GmbH, Krefeld, Germany). The DIC camera had a resolution of 12 MP, and images were acquired at a frequency of 2 Hz. Calibration was performed using the corresponding calibration target. To enable DIC, the specimen surface was prepared using a light primer and a dark speckle pattern, as shown in Fig. 6. The DIC recordings were intended to provide both global and local kinematic information, with particular emphasis placed on the relative displacement between inner and outer adherents in the joint region.

2.4.3. Failure definition and termination criteria

Failure initiation was defined as the first point at which the slope of the force–machine displacement response became negative under displacement control. This criterion was employed as the primary event for terminating the initial loading phase and for defining a comparable state across specimens. The tests were generally continued until this criterion was reached and were then extended to a minimum machine displacement of 4 mm; selected tests were continued further to document post-peak response and to support post-test inspection.

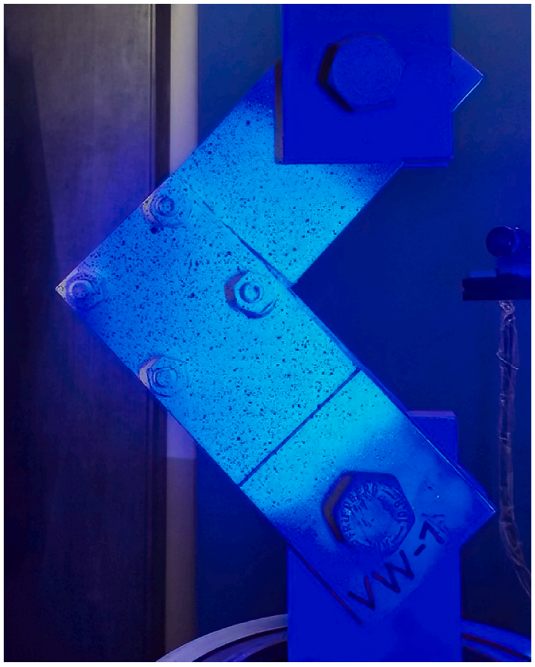

Fig. 6. Representative specimen ready for testing; blue illumination for DIC measurements. (For interpretation of the references to colour in this figure legend, the reader is referred to the web version of this article.)

3. Results

3.1. Load–deformation behaviour

For preliminary considerations and rapid cross-series comparison, the machine-recorded load–displacement curves shown in Fig. 7 were evaluated and the subsequently auxiliary quantities were summarised in Table 3. Herein, GV denotes the slip-resistant bolted reference joint, whereas SD and SW denote the hybrid joints combining pretensioned bolts and an adhesive layer (SD: Sikadur 370; SW: SW7240). To complement the machine-based assessment, the same descriptor set was also derived from digital image correlation (DIC)-based load–relative-displacement curves, thereby expressing the response in joint kinematics and filtering out machine compliance.

It is noted that the following load–deformation characteristics are obtained for a complex-shear joint typology (rotation- and contact-driven), thereby extending commonly reported lap-joint evidence to a connection configuration with coupled shear–normal bondline loading.

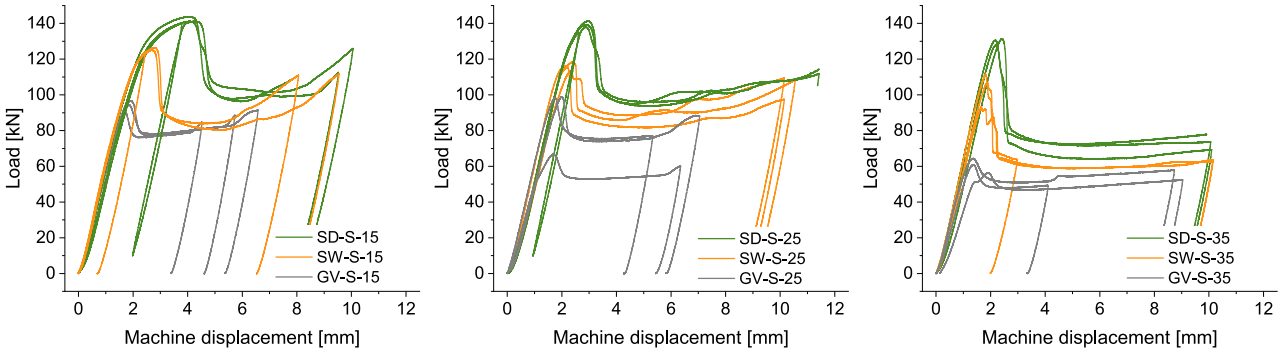

(a) $e = 15$ mm. (b) $e = 25$ mm. (c) $e = 35$ mm.

Fig. 7. Load–deformation behaviour of the S-series (outer splice plate thickness $t_o = 10$ mm) for $e = 15$, 25, and 35 mm, plotted as load versus machine-based absolute displacement.

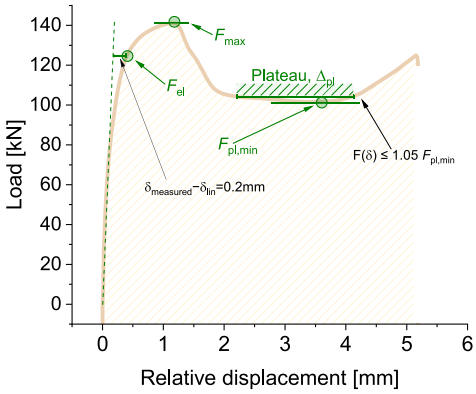

Fig. 8. Definition of the load–displacement descriptors used for the staged-response characterisation. The elastic–deviation point F_{el} is defined by a displacement deviation of 0.2 mm from the linear-elastic extrapolation. The peak load F_{max}, the minimum plateau load $F_{pl,min}$, and the plateau width $\Delta\delta_{pl}$ are determined from the post-peak response, with $\Delta\delta_{pl}$ defined as the displacement interval satisfying $F(\delta) \leq 1.05\, F_{pl,min}$. The work W corresponds to the area under the load–displacement curve, indicated by the hatched region.

The machine-recorded load–displacement curves in Fig. 7 followed a recurring pattern comprising an initially quasi-linear rise, a gradual transition to reduced stiffness as the response approached the maximum load F_{max}, and a distinct post-peak load drop into a plateau-like regime with an approximately sustained load level $F_{pl,min}$. In this representation, the displacement corresponds to the machine crosshead displacement, denoted δ_m, as illustrated in Fig. 8. For a given edge distance, the hybrid configurations generally reached higher F_{max} values than the GV reference, while also retaining higher residual load levels $F_{pl,min}$; within the hybrids, SD typically exceeded SW.

The departure from linear-elastic behaviour was characterised by the elastic-deviation point (F_{el}, δ_{el}) and the associated stiffness K_{el} (Table 3). The elastic-deviation point is used herein as an operational descriptor for the onset of measurable non-linearity under monotonic loading. In the hybrid configurations, a clear deviation from the initial linear trend was typically observed already in the pre-peak regime, reflecting a progressive stiffness loss prior to reaching F_{max}. By contrast, for the largest edge distance in the S-series the deviation criterion was not met before F_{max}, indicating that the response remained close to the initial linear trend up to peak within the adopted tolerance. For series marked with * in Table 3, the deviation criterion was not satisfied before peak load, and the elastic-deviation load therefore coincided with F_{max}. For series marked with $^+$, the adapted evaluation was applied only to a single specimen.

For a finer evaluation, the elastic-deviation load F_{el} was defined as the first point on the load–displacement curve at which the machine displacement deviated by more than 0.2 mm from a straight-line fit to $\delta_m(F)$ between 20 kN and $0.8F_{max}$. The lower fit boundary of 20 kN was selected to avoid the initial seating and alignment phase. The corresponding displacement was denoted δ_{el}, and the associated stiffness was calculated as $K_{el} = F_{el}/\delta_{el}$. The post-peak plateau quantities were obtained from the same load–displacement curves after reaching F_{max} by identifying the minimum plateau load $F_{pl,min}$, the corresponding displacement $\delta_{pl,min}$, and a plateau length defined as the displacement interval in which the load remained within 5% above $F_{pl,min}$.

The extent of the plateau was reflected by a finite displacement range $\Delta\delta_{pl}$ (Table 3). In general, the hybrids exhibited a more developed plateau than the GV reference. Within the S-series, the plateau tended to extend over a wider displacement range with increasing edge distance, consistent with a more prolonged post-peak deformation regime at larger e. In the M/L series, the plateau extent was comparatively shorter, indicating a more confined post-peak displacement development. Herein, "plateau" refers to the post-peak load-carrying region following the first pronounced drop, as quantified by $F_{pl,min}$, $\delta_{pl,min}$, and $\Delta\delta_{pl}$.

Table 3 summarised the machine-based descriptors and enabled a direct comparison with GV as reference within the S-series. Overall, hybridisation increased the characteristic load levels in a consistent manner, with SD generally exceeding SW. In the following, "increase" refers to changes of the mean values, while the reported standard deviations provide a context for the relative separation between series.

At $e = 15$ mm, the increase in peak capacity was already pronounced: F_{max} exceeded the GV level by about +51% for SD and +33% for SW. The post-peak plateau was affected in the same direction but less strongly, with $F_{pl,min}$ increased by about +28% (SD) and +7% (SW). A similar picture emerged from the deviation-from-linearity descriptor, with F_{el} higher than GV by about +33% (SD) and +27% (SW), while K_{el} remained close to the reference.

At $e = 25$ mm, the relative gains in F_{max} persisted (+57% for SD and +32% for SW), and the increase in the plateau level became more distinct (+41% for SD and +27% for SW). The strongest separation with respect to GV was observed in F_{el}, which rose by about +54% (SD) and +34% (SW), accompanied by an increase in K_{el} of about +8% and +5%, respectively.

At $e = 35$ mm, the advantages of hybridisation remained pronounced. Relative to GV, F_{max} increased by about +114% for SD and +71% for SW, while $F_{pl,min}$ increased by about +43% and +22%, respectively. In addition, the plateau widened substantially, with $\Delta\delta_{pl}$ increasing by about +74% (SD) and +97% (SW). For this edge distance, the deviation criterion was not met before F_{max} in the hybrids (values marked with *), such that F_{el} coincided with F_{max} and K_{el} was reported as a peak-point stiffness proxy rather than as an elastic-deviation stiffness measure.

Table 3
Means and standard deviations for the maximum load F_{max}, the elastic-deviation point (F_{el}, δ_{el}, K_{el}), and the post-peak plateau ($F_{pl,min}$, $\delta_{pl,min}$, $\Delta\delta_{pl}$) as determined from the machine measurements.

Series	F_{max} [kN]	F_{el} [kN]	δ_{el} [mm]	K_{el} [kN/mm]	$F_{pl,min}$ [kN]	$\delta_{pl,min}$ [mm]	$\Delta\delta_{pl}$ [mm]
GV-S-15^{+}	93.81 ± 2.80	93.65 ± 2.63	1.80 ± 0.08	52.09 ± 0.93	76.99 ± 0.81	2.60 ± 0.29	2.38 ± 0.41
GV-S-25^{+}	88.07 ± 15.06	85.79 ± 18.28	1.70 ± 0.26	50.01 ± 5.03	67.27 ± 10.27	3.30 ± 0.17	3.52 ± 0.21
GV-S-35^{+}	60.63 ± 3.29	57.54 ± 8.82	1.41 ± 0.18	41.42 ± 11.38	48.37 ± 1.81	2.88 ± 0.34	3.04 ± 0.55
SD-S-15	141.70 ± 1.56	124.75 ± 0.70	2.43 ± 0.08	51.29 ± 1.95	98.43 ± 2.17	6.23 ± 0.60	3.13 ± 0.93
SD-S-25	138.68 ± 2.40	132.28 ± 0.96	2.44 ± 0.02	54.17 ± 0.39	94.74 ± 0.82	5.01 ± 0.31	2.97 ± 0.47
SD-S-35*	130.00 ± 1.40	/	2.27 ± 0.11	57.49 ± 2.46	69.24 ± 3.65	5.48 ± 0.15	5.28 ± 0.20
SW-S-15	125.18 ± 0.92	118.92 ± 0.50	2.19 ± 0.02	54.40 ± 0.33	82.00 ± 1.88	4.89 ± 0.38	2.50 ± 0.04
SW-S-25	115.96 ± 2.04	114.74 ± 1.07	2.18 ± 0.12	52.72 ± 3.22	85.21 ± 2.82	4.50 ± 0.38	3.22 ± 0.75
SW-S-35*	103.97 ± 7.69	/	1.79 ± 0.10	58.19 ± 2.11	58.78 ± 0.09	4.97 ± 0.05	5.98 ± 0.63
SD-M-15	150.17 ± 3.85	128.17 ± 1.21	2.23 ± 0.03	57.47 ± 0.26	105.21 ± 1.45	5.56 ± 0.12	1.73 ± 0.05
SD-L-15	148.49 ± 2.42	125.23 ± 1.22	2.07 ± 0.06	60.70 ± 1.98	104.57 ± 3.85	6.13 ± 0.50	2.57 ± 0.16
SW-M-15	134.41 ± 1.47	124.43 ± 0.92	2.11 ± 0.00	58.84 ± 0.50	90.62 ± 3.61	4.37 ± 0.57	2.43 ± 0.00
SW-L-15	134.26 ± 4.82	124.77 ± 2.90	2.01 ± 0.08	62.14 ± 0.97	90.80 ± 0.21	4.89 ± 0.16	2.32 ± 0.21

* indicates almost linear-elastic behaviour up to F_{max}, with δ_{el} evaluated at F_{max} and $K_{el} = F_{max}/\delta_{el}$ reported as a peak-point stiffness proxy. $^{+}$ indicates that the adapted evaluation was done for only a single specimen.

Table 4
Means and standard deviations for the maximum load F_{max}, the elastic-deviation point (F_{el}, δ_{el}, K_{el}), and the post-peak plateau ($F_{pl,min}$, $\delta_{pl,min}$, $\Delta\delta_{pl}$) as determined from DIC measurements.

Series	F_{max} [kN]	F_{el} [kN]	δ_{el} [mm]	K_{el} [kN/mm]	$F_{pl,min}$ [kN]	$\delta_{pl,min}$ [mm]	$\Delta\delta_{pl}$ [mm]
GV-S-15^{+}	93.81 ± 2.80	93.62 ± 2.60	0.38 ± 0.04	249.89 ± 22.09	77.14 ± 0.78	1.03 ± 0.06	1.65 ± 0.26
GV-S-25^{+}	88.07 ± 15.06	85.73 ± 18.37	0.33 ± 0.03	259.38 ± 61.51	68.04 ± 10.75	1.32 ± 0.39	1.53 ± 0.88
GV-S-35^{+}	60.63 ± 3.29	58.74 ± 7.13	0.29 ± 0.04	206.22 ± 41.55	48.47 ± 1.76	1.23 ± 0.19	1.92 ± 0.36
SD-S-15	141.70 ± 1.56	130.25 ± 1.05	0.50 ± 0.00	258.35 ± 0.81	98.57 ± 2.18	2.85 ± 0.38	2.13 ± 0.65
SD-S-25	138.68 ± 2.40	137.79 ± 3.08	0.52 ± 0.01	262.75 ± 1.58	94.90 ± 0.88	2.26 ± 0.25	1.97 ± 0.33
SD-S-35*	130.00 ± 1.40	/	0.35 ± 0.01	375.25 ± 10.50	69.40 ± 3.71	2.75 ± 0.17	3.37 ± 0.11
SW-S-15^{+}	125.18 ± 0.92	123.22 ± 0.90	0.54 ± 0.00	229.47 ± 0.50	82.12 ± 1.82	2.40 ± 0.21	1.71 ± 0.00
SW-S-25^{+}	115.96 ± 2.04	115.57 ± 2.54	0.48 ± 0.02	242.24 ± 15.20	85.38 ± 2.80	2.16 ± 0.33	2.52 ± 0.23
SW-S-35*	103.97 ± 7.69	/	0.29 ± 0.03	362.92 ± 66.29	58.85 ± 0.09	2.60 ± 0.06	3.81 ± 0.37
SD-M-15	150.17 ± 3.85	134.52 ± 3.18	0.52 ± 0.01	260.84 ± 1.68	105.32 ± 1.46	2.59 ± 0.02	1.17 ± 0.04
SD-L-15	148.49 ± 2.42	131.38 ± 1.94	0.51 ± 0.01	258.98 ± 1.00	104.71 ± 3.90	3.01 ± 0.39	1.70 ± 0.10
SW-M-15	134.41 ± 1.47	133.00 ± 0.83	0.57 ± 0.00	234.26 ± 0.23	90.75 ± 3.63	2.01 ± 0.46	1.70 ± 0.01
SW-L-15	134.26 ± 4.82	134.71 ± 3.62	0.57 ± 0.01	235.17 ± 1.55	90.92 ± 0.22	2.39 ± 0.01	1.58 ± 0.13

* indicates almost linear-elastic behaviour up to F_{max}, with δ_{el} evaluated at F_{max} and $K_{el} = F_{max}/\delta_{el}$ reported as a peak-point stiffness proxy. $^{+}$ indicates that the adapted evaluation was done for only a single specimen.

When the reported scatter was considered, the separations in F_{max} and $F_{pl,min}$ between GV and the hybrids were generally large compared with the within-series variability of SD and SW, which suggested that the observed differences were unlikely to be governed by random scatter alone. Nevertheless, the higher variability of GV in parts and the presence of adapted values implied that these findings should be interpreted as robust trends in an engineering sense rather than as statistically definitive outcomes.

3.1.1. DIC measurements

Figs. 10 and 11 present the load–deformation response expressed in terms of DIC-based relative displacement, thereby filtering out machine compliance and focusing on the joint kinematics. The evaluated gauge points and the displacement quantity used for the DIC-based evaluation are shown in Fig. 9. The relative displacement Δx was evaluated between gauge points located on the inner and outer adherends in the overlap region and was taken orthogonal to the outer-splice edge. This displacement quantity is denoted δ_{rel} in the following.

In Fig. 10, the S-series responses for $e = 15$, 25, and 35 mm showed a qualitatively similar staged behaviour to that observed in the machine-based representation, but with a clearer separation of the kinematic phases. An initially steep rise in load at very small relative displacements was followed by a progressive reduction in slope towards the maximum load F_{max}. The subsequent first pronounced load drop occurred at relatively small relative displacements, after which a quasi-stationary post-drop branch developed at an approximately constant load level. Compared with the machine-based representation, the DIC-based curves indicate substantially smaller characteristic displacements at comparable load levels, consistent with the removal of machine compliance. In the following, this reduction is referred to as a “kinematic contraction” relative to δ_m, without implying a change in the underlying load levels. In this representation, the hybrid configurations exhibited consistently smaller relative displacements at comparable load levels than the GV reference, indicating a more effective constraint of joint opening and slip. For a given edge distance, SD reached higher loads at slightly larger relative displacements than SW, suggesting a more extended redistribution phase prior to the first pronounced transition. Increasing edge distance led to a systematic reduction in both peak and plateau load levels and to a broader spread of post-drop trajectories, consistent with a more pronounced rotation-driven deformation mechanism.

For completeness, the descriptor trends from Table 4 are summarised once in the present section, to avoid repetition between the machine- and DIC-based representations. Table 4 exhibits the same qualitative ordering as the previous machine-based descriptor table. In the S-series, hybridisation consistently increases the characteristic load levels, with F_{max} and $F_{pl,min}$ being higher for SD and SW than for GV at the same edge distance, and SD tending to exceed SW. In loose statistical terms, these separations appear robust because the mean shifts are generally

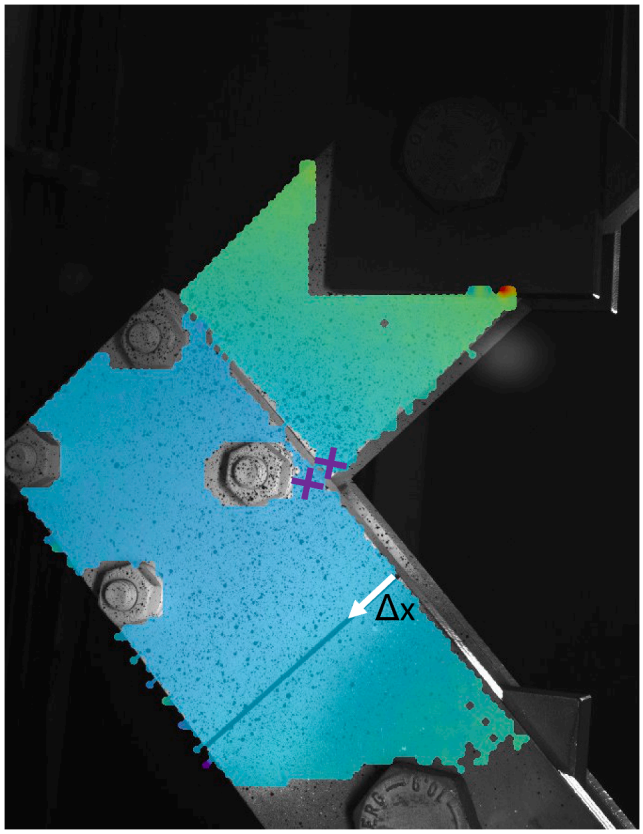

Fig. 9. Gauge points and evaluated displacement for DIC measurements.

large relative to the within-series scatter of SD/SW, whereas the GV series exhibits noticeably higher scatter, which weakens strict significance claims for selected comparisons without changing the overall trend.

The elastic-deviation descriptor follows the same pattern, i.e. F_{el} increases from GV to the hybrids and often tracks $F_{\max}$. For series marked with *, F_{el} coincides with $F_{\max}$, such that the descriptor indicates an approximately linear response up to peak within the adopted criterion rather than an earlier deviation point. Compared with the machine-based table, the characteristic displacements δ_{el} and $\delta_{pl,\min}$ are reduced in magnitude, and consequently the derived stiffnesses K_{el} are increased, which is consistent with the removal of machine compliance in the relative-displacement representation. The plateau trends remain comparable to the machine-based evaluation: the hybrids retain higher post-drop levels than GV, while differences in plateau extent $\Delta\delta_{pl}$ appear less pronounced and more affected by scatter than differences in plateau level.

3.1.2. Hysteresis tests

Hysteresis tests were not conducted systematically across the experimental programme but were applied only to a limited subset of specimens; in particular, no GV series was investigated under cyclic unloading–reloading. The subset selected for hysteresis investigation comprised (i) SD specimens (Sikadur 370) in the S-series at $e = 15$ mm, $e = 25$ mm, and $e = 35$ mm, and (ii) SW specimens (SW7240) in the L-configuration within the thickness comparison. It is emphasised that the locations of the unloading–reloading segments were prescribed within the test procedure and therefore should not be interpreted as mechanically emergent "hysteresis onsets".

For SD at $e = 15$ mm and $e = 25$ mm, unloading was initiated at a load of 130 kN, followed by displacement-controlled unloading until 10 kN, after which reloading was continued until test abortion. At $e = 35$ mm, the loop was initiated at 70 kN and likewise unloaded to 10 kN prior to reloading. The resulting SD loops at $e = 15$ mm and $e = 25$ mm were broadly comparable in shape and opening, whereas the loop at $e = 35$ mm exhibited a smaller opening, consistent with the lower upper-bound load level and the associated lower displacement excursion between 70 kN and the 10 kN boundary.

For SW7240 in the L-configuration (Fig. 11b), multiple loops were conducted at different stages of the test: prior to the onset of macroscopic slip at approximately 70 kN, 120 kN, and 130 kN, as well as directly after slipping and twice more during the post-slipping plateau. Across these cycles, the loop shapes remained largely similar, with only a slight tendency towards more open loops at higher load and displacement levels. Overall, the enclosed areas of the identifiable loops remained small relative to the work input up to the first pronounced load drop, such that the energy dissipated within the loops stayed below 1% of the total energy dissipated up to failure. Consequently, comparisons between loop energies primarily reflected differences associated with the prescribed load and displacement levels at which cycling was applied (i.e. loop position), while any adhesive-related influence could only be inferred as a secondary effect within the limited dataset; for SW7240 in particular, no robust position-dependent trend beyond the slight increase in loop opening at higher levels was established from the plotted responses.

Notably, the progressive shift of the loop position—and thus of the displacement attained at the lower boundary load of 10 kN—was observed already prior to the onset of macroscopic slip. This indicated that irreversible deformation accumulated before slipping occurred. Since the bond was still intact at that stage, the associated plasticity was attributed primarily to local yielding of the adherents rather than to adhesive degradation.

3.2. Failure patterns and post-test observations

The governing failure mechanisms are assessed by post-test inspection of the contact and fracture surfaces, with emphasis placed on the hybrid joints (SD and SW) and on the slip-resistant bolted joints (GV) being used as a mechanical reference. Across all series, the macroscopic response stages described in Section 3.1 are reflected by characteristic surface signatures after testing, i.e. by abrasion patterns on the galvanised surfaces, by imprint and residue patterns on the adhesive-covered regions, and by localised surface damage features in the vicinity of the bolt holes. The observations discussed below are aligned with the concept-dependent differences in peak and post-drop response reported in Tables 3 and 4. In this subsection, "contact surfaces" refers to the faying surfaces in the overlap, whereas "fracture surfaces" refers to the separated adherend surfaces after debonding.

For the GV series, the dominant post-test signature is a pronounced abrasion of the zinc layer in the vicinity of the bolt holes, whereas the central overlap region exhibits little to no abrasion (Fig. 12a). The wear is concentrated around the fasteners and appears as bright, rubbed zones, while the overlap centre remains comparatively unchanged. The abrasion intensity differs between the two adjacent surfaces, with the right one in Fig. 12a appearing much blunter.

For both hybrid concepts, fracture surfaces indicate adhesive failure at the zinc-coated interface (Fig. 12b and c). Adhesive residues are present on both separated adherends, and the residual coverage is patchy, with localised residue islands outside the main imprint. The bonded overlap region is delineated by a recognisable imprint area, within which smear marks and abrasion tracks are visible on the adhesive surface. Along the overlap length, the disturbance of residues and the abrasion intensity vary spatially, and the markings are more pronounced at the edges and especially in the area close to the inner bolt. In the inspected hybrid specimens, no bolt shear failure and no bolt-hole bearing failure are observed, and no gross tear-out of the steel plates is documented. The bolt-hole region does not exhibit a continuous adhesive infill; instead, only local adhesive remnants are observed at the hole edge and on the adjacent contact surfaces.

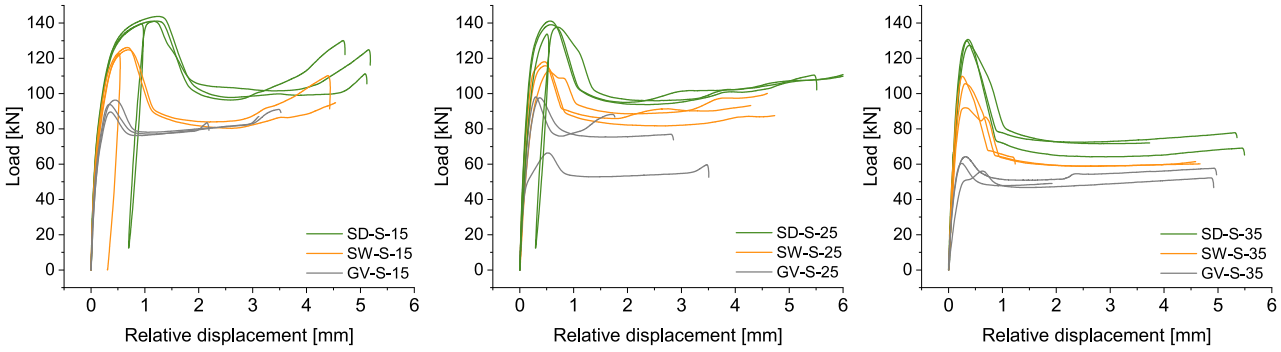

(a) $e = 15$ mm. (b) $e = 25$ mm. (c) $e = 35$ mm.

Fig. 10. Load–deformation behaviour of the S-series ($t_o = 10$ mm) for $e = 15$, 25, and 35 mm, plotted as load versus DIC-based relative displacement.

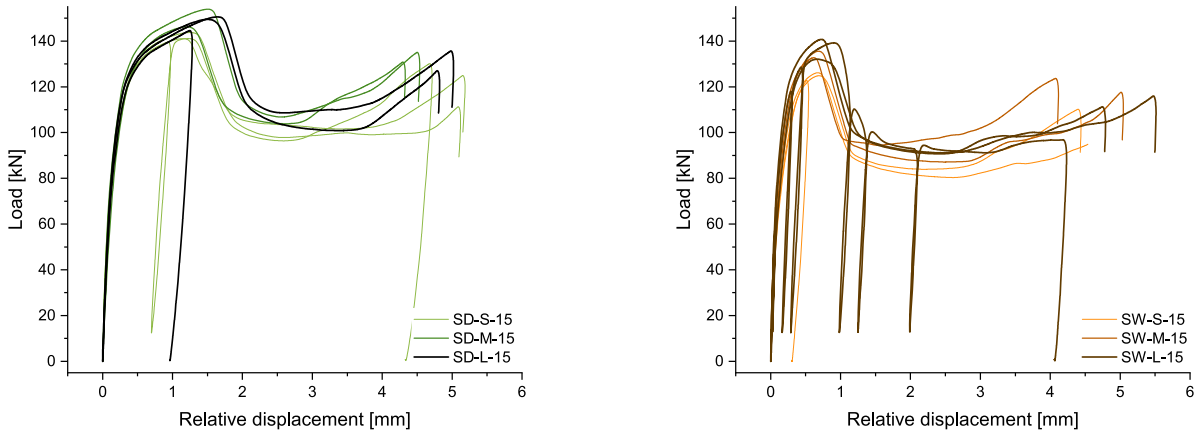

(a) SD370. (b) SW7240.

Fig. 11. Influence of outer splice plate thickness ($t_o = 10$, 15, and 20 mm) on the relative displacement response at $e = 15$ mm.

Between the two adhesives, differences in the fracture-surface appearance are observed. For SD370 (Fig. 12b), the imprint boundary is locally more distinct, and residue-free zones and residue-covered zones are more clearly separated. Adhesive squeeze-out is visible along the overlap boundary. For SW7240 (Fig. 12c), the imprint region remains clearly identifiable, while the abraded areas appear more uniformly "polished" and fine abrasion patterns are visible, with locally detached fragments near the imprint perimeter. In the documented images, no cohesive fracture through the adhesive thickness is visually apparent for either adhesive.

3.2.1. *Tests aborted prior to failure*

In order to inspect the state of the bondline at defined stages of the loading history, selected hybrid-joint tests are stopped shortly before the expected maximum load and are subsequently unloaded. After removal from the rig and loosening of the bolts, the adherents are observed to remain bonded and to require substantial peel loading for forcible separation. The corresponding load–machine-displacement curves (not shown here) follow the same qualitative response path up to the interruption point. Post-test observations are summarised in Fig. 13. The term "aborted" is used herein to denote tests stopped prior to the global load drop associated with failure.

The SD-L-15-3 specimen is stopped at roughly 145 kN and is unloaded. A residual machine displacement of about 1.8 mm is reported after unloading. After separation of the adherends, localised damage features are visible on the contact surfaces within the overlap (Fig. 13a). Tear-offs of the zinc coating are observed at the bolt holes, including in the vicinity of the inner bolt hole.

For SW7240, the SW-S-15-3 specimen is stopped at approximately 120 kN and is unloaded. A residual machine displacement of about 0.7 mm is reported after unloading. The adherents remain bonded and require forcible separation. The resulting contact-surface appearance is shown in Fig. 13b.

4. Discussion

The discussion is framed by the motivation and boundary conditions introduced in Sections 1–2 and by the response descriptors reported in Section 3.1 (Figs. 7–11, Tables 3, and 4). As a reminder, GV denotes the slip-resistant bolted reference joint, whereas SD and SW denote hybrid joints combining pretensioned bolts and an adhesive layer (SD: Sikadur 370; SW: SW7240); and *hybridisation* is defined as the deliberate combination of a pretensioned slip-resistant bolted friction joint with an adhesive-bonded overlap, such that frictional transfer, bolt-induced confinement, and adhesive shear transfer act concurrently and evolve with increasing rotation [16,17]. Where appropriate, statistical significance claims are supported by two-sided Welch t-tests [33].

4.1. *Relative performance of joining concepts*

Hybridisation was associated with pronounced increases in peak resistance relative to the GV reference across the S-series. For F_{max}, the comparison between GV and SD was significant at all investigated edge distances[1]. The comparison between GV and SW was significant at $e = 15$ mm[2] and $e = 35$ mm[3], whereas at $e = 25$ mm this comparison was

[1] For $e = 15$ mm: $\Delta = +45.36$ kN; 95% CI: 39.61–51.11 kN; $p = 1.1 \times 10^{-4}$; for $e = 35$ mm: $\Delta = +69.37$ kN; 95% CI: 62.37–76.37 kN; $p = 1.3 \times 10^{-4}$.

[2] $\Delta = +28.84$ kN; 95% CI: 22.62–35.06 kN; $p = 1.4 \times 10^{-3}$.

[3] $\Delta = +43.34$ kN; 95% CI: 26.99–59.69 kN; $p = 4.3 \times 10^{-3}$.

(a) GV-S-15: representative sliding surfaces after testing, showing abrasion of the zinc layer concentrated around the bolt holes and limited abrasion in the central overlap region.

(b) SD-S-15: representative fracture surfaces after testing, indicating adhesive failure at the zinc-coated interface and abrasion marks within the adhesive layer.

(c) SW-S-15: representative fracture surfaces after testing, indicating adhesive failure at the zinc-coated interface and abrasion marks within the adhesive layer; no dominant bolt shear or bolt-hole bearing failure was identified in the inspected specimens.

Fig. 12. Representative post-test surface signatures.

not statistically supported at the adopted level. For the post-drop minimum plateau load $F_{pl,min}$, the comparison between GV and SD was significant at $e = 15$ mm[4] and $e = 35$ mm[5], while the comparison between GV and SW reached significance at $e = 35$ mm only[6]. The same ranking was reflected in the scatter, with the GV reference exhibiting markedly higher variability at $e = 25$ mm than the hybrid series. This contrast in scatter is consistent with the post-test surface signatures (Section 3.2), which show localised abrasion around bolt holes for GV, whereas the hybrids exhibit imprint and residue patterns distributed over the bonded overlap, indicating a more distributed participation of the overlap region in load transfer.

Taken together, the results were considered consistent with preloaded hybrid-joint mechanics, in which the bonded transfer path

[4] $\Delta = +21.44$ kN; 95% CI: 15.65–27.23 kN; $p = 2.1 \times 10^{-3}$.
[5] $\Delta = +20.87$ kN; 95% CI: 11.55–30.19 kN; $p = 5.9 \times 10^{-3}$.
[6] $\Delta = +10.41$ kN; 95% CI: 4.92–15.90 kN; $p = .015$.

(a) SD-L-15-3: contact surfaces after forcible separation.

(b) SW-S-15-3: contact surfaces after forcible separation.

(c) Detail view: bolt hole with local tear-off of the zinc coating.

Fig. 13. Post-test inspection of specimens stopped prior to failure.

and bolt-induced confinement provide an additional distributed load-transfer mechanism that predominantly amplifies peak resistance, whereas post-drop resistance remains more sensitive to evolving contact conditions and coating-governed interface processes [4,16,17]. The reduced scatter observed for the hybrid series was interpreted as indicative of a stabilising effect that has repeatedly been reported for preloaded hybrid joints, reflecting reduced susceptibility to localised interface variability compared with friction-only connections [4,17]. This interpretation is supported by the fracture patterns: for SD and SW, adhesive residues were observed on both adherends and the bonded region remained identifiable by an imprint area (Section 3.2), whereas GV exhibited limited abrasion in the overlap centre, indicating that frictional mobilisation remained concentrated near fasteners.

4.2. Joining-concept effects under complex shear

In the following, the term *joining concept* referred to the governing load-transfer mechanism realised by the connection, i.e. the friction-dominated bolted reference (GV) versus the hybrid configurations combining frictional transfer, bolt-induced confinement, and adhesive bonding (SD and SW).

Across the investigated parameter range, the hybrid joining concepts exhibited a systematic shift of the elastic-deviation point towards higher load levels at $e = 15\,\mathrm{mm}$ and $e = 25\,\mathrm{mm}$ compared with the GV reference (Table 3), while the corresponding elastic stiffness K_{el} remained of comparable magnitude. In this context, the elastic-deviation point (F_{el}, δ_{el}) is an operational descriptor that marks the onset of measurable non-linearity under monotonic loading, while $K_{el} = F_{el}/\delta_{el}$ provides a

stiffness proxy at that point. At $e = 35$ mm, the deviation criterion was not met before reaching F_{max} for either hybrid configuration (values marked by ⋆), such that stiffness-based deviation measures no longer discriminated between joining concepts. For the ⋆-marked series, δ_{el} was taken at the peak point so that $K_{el} = F_{el}/\delta_{el}$ could be reported as a peak-point stiffness proxy rather than as a deviation-based stiffness descriptor. Under these conditions, post-drop descriptors became dominant: the plateau length $\Delta\delta_{pl}$ increased from 3.04 mm for GV-S-35 to 5.28 mm for SD-S-35 and 5.98 mm for SW-S-35, while the minimum plateau load $F_{pl,min}$ increased from 48.37 kN to 69.24 kN and 58.78 kN, respectively. At smaller edge distance ($e = 15$ mm), the displacement at the onset of the post-drop plateau was substantially larger for the hybrid configurations than for the GV reference (Table 3).

These trends were interpreted as indicating that hybridisation modified the redistribution pathway in complex shear rather than merely scaling characteristic load levels. The DIC-based load–relative-displacement curves confirm the staged response while indicating smaller characteristic displacements at comparable load levels, consistent with the removal of machine compliance and with a kinematic separation of phases (Fig. 10). The upward shift of the elastic-deviation point was taken to reflect a prolonged quasi-linear regime in the hybrid configurations, consistent with progressive load redistribution among frictional transfer, bolt-induced confinement, and adhesive shear prior to the first pronounced transition. The reduced discriminative power of the deviation criterion at $e = 35$ mm was interpreted as a limitation of stiffness-based measures for responses remaining near-linear up to peak, implying that peak and post-peak descriptors provide a more robust basis for comparing joining concepts in this configuration. The combined increase in $F_{pl,min}$ and $\Delta\delta_{pl}$ at $e = 35$ mm was interpreted as a quantitative manifestation of enhanced post-drop robustness, in line with observations reported for preloaded hybrid joints [4,17]. The post-test observations are compatible with this enhanced post-drop robustness: after failure, imprint and abrasion patterns remained visible over the bonded overlap for SD and SW, indicating continued contact and relative motion on the fractured adhesive surfaces (Section 3.2).

4.3. Geometry-driven kinematics

Edge distance reduced peak resistance for all concepts, but the reduction was substantially stronger for GV than for SD and SW (Table 3). At the same time, post-drop deformation capacity increased markedly with edge distance for the hybrids, as reflected by the substantial growth of $\Delta\delta_{pl}$ at $e = 35$ mm relative to GV. The DIC-based representation further indicates that, at comparable load levels, the hybrids exhibit smaller relative displacements than GV, consistent with a stronger constraint of joint opening/slip (Fig. 10). For the thickness series at $e = 15$ mm, F_{max} increased only modestly from S to M/L for both adhesives, whereas $\Delta\delta_{pl}$ was strongly reduced for SD (most notably in the M-configuration) and only weakly reduced for SW. The post-test surface signatures remained qualitatively similar across these geometric variants, i.e. GV exhibited bolt-region abrasion on galvanised steel, whereas the hybrids exhibited interfacial debonding with imprint and residue patterns, indicating that parameter changes modified the kinematic development without altering the governing failure locus (Section 3.2).

The reduced edge-distance sensitivity of SD and SW relative to GV might be explained by the differing load-transfer mechanism. The GV series transfer the load exclusively via friction. Here, the resistance is defined by the effective lever arm of the bolts. In this context, the effective lever arm is the distance between the bolt and the centre of mass of the bolt pattern. In contrast, the hybrid series' specimens transfer load via adhesive bonding, too. As the edge-distance sensitivity is low, the performance of the load transfer seems to be mostly defined by the polar moment of inertia of the adhesive layer, which is similar for all investigated edge distances. Therefore, increasing the effective lever arm only leads to slight improvements of the performance of the hybrid specimens. The modest peak-level thickness gains were interpreted as indicating that F_{max} approaches a local-interface-controlled saturation regime once global compliance is reduced. In this sense, edge distance and outer-plate thickness are interpreted primarily as modifiers of rotation and contact evolution, which shape the redistribution pathway into the post-drop regime. The pronounced thickness sensitivity of $\Delta\delta_{pl}$ for SD was interpreted as evidence that stiffness primarily modifies the redistribution pathway and post-drop kinematics by altering the rotation pathway and the evolution of local normal-stress distributions, rather than by increasing the intrinsic interface strength.

4.4. Unloading loops and irreversibility

Cyclic unloading–reloading was applied only to a limited subset of specimens and was not used for population-level inference; no GV series was investigated under cycling. Within the investigated subset, loop openings for SD at $e = 15$ mm and $e = 25$ mm were reported as comparable, while SW in the L-configuration exhibited largely similar loop shapes across load levels with only a slight tendency towards increased opening at higher load levels.

The loop behaviour was interpreted as compatible with mixed mechanisms discussed for preloaded hybrids [17], in which partial recoverability is associated with frictional closure and re-engagement, while irreversible kinematic accumulation is associated with progressive interfacial degradation and/or local plasticity. Because loop metrics (e.g. dissipated energy, residual displacement per loop, unloading/reloading stiffness) were not derived, statistical inference was not advanced for cyclic behaviour, and the evidence was treated as qualitative support for irreversibility under mixed friction–bonding action. The post-test inspection of specimens stopped prior to failure further indicates that localised interfacial activity and local coating tear-off at bolt holes can occur prior to global collapse (Section 3.2.1), which is consistent with the presence of irreversible mechanisms already in the pre-peak regime.

4.5. Multiaxial strength characterisation as an explanatory lens

Hybrid joints under complex shear were expected to develop coupled shear and normal stresses in the bondline due to pretension, eccentricity, and rotation. Multiaxial adhesive strength characterisation on galvanised steel was therefore retained as an explanatory lens, while recognising that bulk and coupon-scale properties are not sufficient predictors for hybrid-joint performance, which is governed by an evolving interaction between bonding, confinement, and contact.

Reference data indicate that SD370 and SW7240 were similar in strength (bulk tensile and lap-shear, including on galvanised steel), while differing mainly in compliance, with SW7240 exhibiting a lower E and higher ε_b (Table 1). Off-axis tests on galvanised steel were reported to yield comparable envelope shapes for both adhesives (bilinear in (σ, τ) and near-linear in (σ_P, σ_1)), but with approximately twofold larger scatter for SW7240 [29]. This indicates that, even under nominally similar combined stress states, SW7240 exhibited a less consistent response than SD370.

In the hybrid joints, SD-based configurations retained higher post-drop load levels at $e = 15$ and $e = 35$ mm, whereas the SW-based configuration exhibited a larger plateau length at $e = 35$ mm (Table 3). The fracture patterns confirm that both hybrid concepts failed by interfacial debonding at the zinc-coated interface, with patchy residue on both adherends and abrasion tracks within the imprint area (Section 3.2), indicating that the difference between SD and SW was expressed through load levels and post-drop development rather than through a change in failure locus. In view of the broadly similar strength envelopes, these differences were interpreted primarily in terms of the evolving stress path in a coupled pressure–tension space, where confinement can delay tensile-driven separation but coating-governed interfacial limitations remain controlling [29]. Within this framing, adhesive compliance was considered a plausible contributor to the dif-

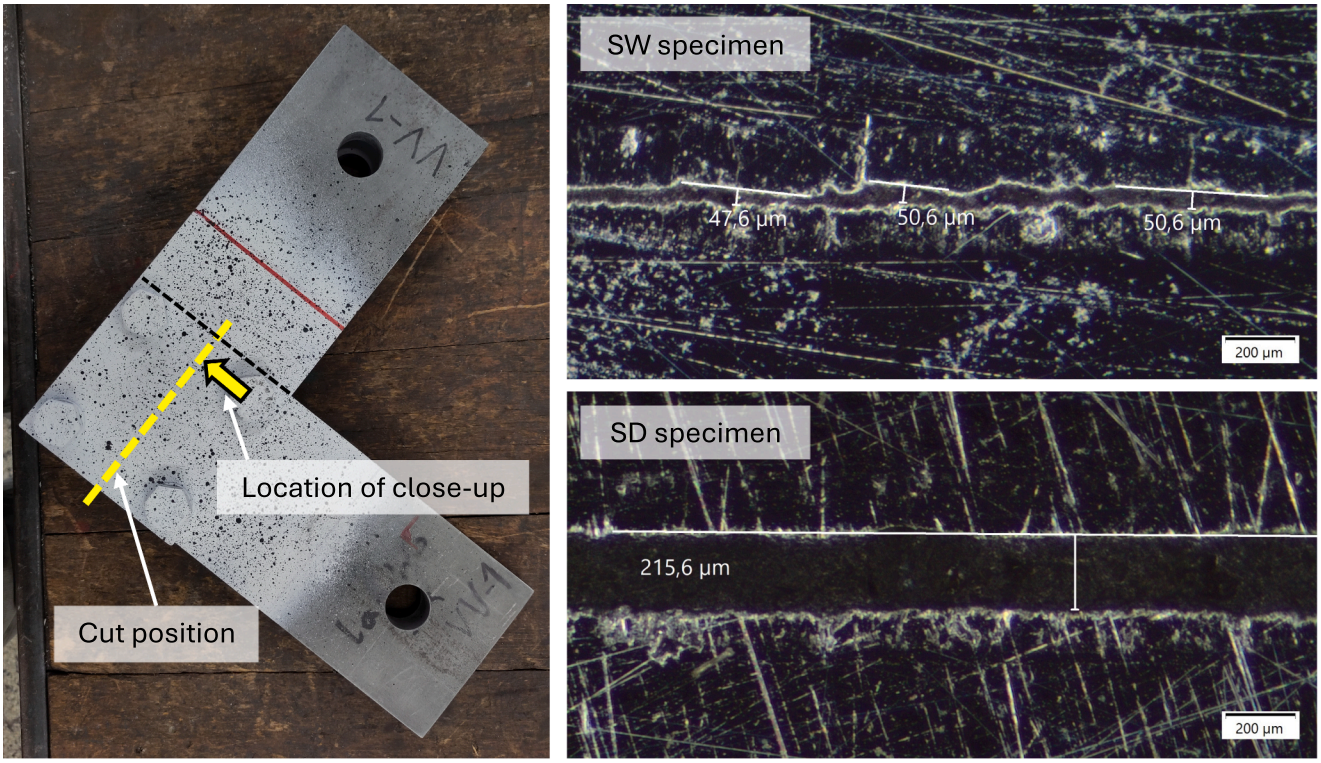

Fig. 14. Location of the cut used for bondline-thickness micrographs and exemplary micrographs for both adhesives.

ferent post-drop developments, while the higher scatter reported for SW7240 under multiaxial characterisation was regarded as a plausible (but non-deterministic) contributor to joint-level variability, particularly in the post-peak regime where local interfacial processes become governing. The resulting interpretation was retained as a working hypothesis and will be evaluated explicitly in the subsequent numerical study.

4.6. Bondline thickness

Across the hybrid series, SD and SW exhibited systematic differences in the machine-based descriptors, with SD generally attaining higher characteristic load levels than SW, while the displacement-based descriptors indicated adhesive-dependent differences in the post-drop development (Table 3). In the S-series, F_{max} and $F_{pl,min}$ were consistently higher for SD than for SW at a given edge distance, and F_{el} tended to be higher for SD where the deviation criterion was met. The initial stiffness proxy K_{el} remained of comparable magnitude for both adhesives, indicating that the main separation between SD and SW was expressed primarily through the load levels and through the subsequent post-drop evolution rather than through a fundamentally different initial elastic slope. The DIC-based descriptors confirm the same qualitative ordering at the level of characteristic loads, while indicating reduced characteristic displacements at comparable load levels, which is consistent with the removal of machine compliance. In the thickness comparison at $e = 15$ mm (S/M/L), both adhesives showed only modest changes in F_{max} with increasing outer splice-plate thickness; however, the post-drop plateau length $\Delta\delta_{pl}$ was markedly reduced for SD (most pronounced in the M-configuration), while remaining comparatively stable for SW, and the plateau onset displacement $\delta_{pl,min}$ remained at higher levels for SD than for SW.

These SD–SW separations were interpreted in view of adhesive-layer thickness differences that arise from processing rather than prescription. To measure bondline thickness, additional untested specimens from series SD-S-15 and SW-S-15 were cut between the bolts. Investigating micrographs (exemplary images displayed in Fig. 14) showed that the bondline thickness for the SD specimen was 200–270 μm, while the SW specimen showed much smaller values (25–60 μm). Under similar geometric and processing conditions, similar bondline thicknesses were reported [31]. The post-test signatures are consistent with the measured thickness contrast in a descriptive sense: SD370 surfaces show more pronounced squeeze-out at overlap edges and locally sharper imprint boundaries, whereas SW7240 surfaces exhibit finer abrasion patterns within the imprint region (Section 3.2). A thicker, more compliant SD bondline was therefore taken to provide a larger scope for kinematic redistribution under rotation and confinement, consistent with (i) the generally higher load levels (F_{max}, F_{el}, $F_{pl,min}$) and (ii) the stronger sensitivity of the post-drop deformation descriptors to the thickness-series boundary conditions. Conversely, the thinner SW bondline was interpreted as limiting compliance-driven kinematic extension and reducing the sensitivity of $\Delta\delta_{pl}$ to splice-plate thickness, such that differences between SW configurations were expressed more as shifts in load levels than as pronounced changes in plateau development. This mechanism-level interpretation aligns with the broader observation that local thickness gradients, particularly near bolt holes, can influence stress concentrations and damage initiation without necessarily governing peak capacity in bolted/bonded hybrids [31].

The mechanism-based interpretation proposed here should be understood as an experimentally supported explanation of the observed response rather than as a fully validated mechanistic model. In particular, the inferred role of rotation-driven localisation is based on the measured load–deformation behaviour, DIC-based displacement trends, and post-test surface observations, but it cannot be separated completely from local contact, frictional interaction, adhesive-thickness variation, and coating-related effects within the present experimental dataset. Accordingly, the dataset is intended to provide a reproducible experimental basis for subsequent model validation and calibration, rather than a standalone validation of the proposed mechanisms.

5. Conclusions

This work investigated the quasi-static behaviour of preloaded bolted–bonded hybrid joints in complex shear on hot-dip galvanised steel under coating-limited interface conditions. A slip-resistant bolted reference (GV) was compared with hybrid joints produced using Sikadur 370 (SD370, *SD*) and Scotch-Weld 7240 (SW7240, *SW*). The effects of joining concept, edge distance e (15, 25, 35 mm) in the *S-series* ($t_o = 10$ mm), and outer splice-plate thickness (S/M/L at $e = 15$ mm) were assessed.

The novelty lay in extending preloaded hybrid-joint evidence from tension-loaded lap-joint benchmarks to a rotation- and contact-driven complex-shear joint typology, and in quantifying peak and post-drop response using consistent descriptor sets derived from machine displacement and DIC-based relative displacement.

Because the sample size of the parametric study was limited and the test matrix was not complete across all parameters, accurate relationships between influencing parameters and load-bearing behaviour could not be derived. Instead, trends were identified.

Across all configurations, a staged response was observed (rise, stiffness reduction, F_{max}, load drop, sustained post-drop branch). The DIC representation confirmed the same staging while indicating smaller characteristic displacements at comparable load levels, consistent with the removal of machine compliance.

Both hybrid concepts attained higher peak and higher post-drop minimum plateau loads than the GV reference, while GV exhibited the strongest edge-distance sensitivity. The thickness series showed only modest changes in F_{max} from S to M/L for both adhesives, whereas the post-drop development was more configuration-dependent, indicating that splice-plate thickness primarily modified the kinematic evolution in complex shear.

SD and SW exhibited a systematic separation: SD generally reached higher characteristic load levels, whereas SW tended to exhibit a more extended post-drop deformation capacity in selected cases. Post-test inspection indicated interfacial debonding at the zinc-coated interface for both adhesives, with imprint/residue patterns distributed over the overlap and without visually dominant bolt shear or bolt-hole bearing failure in the documented series; GV showed localised zinc abrasion concentrated around bolt holes. Manufacturing-driven bondline thickness differences reported for SD370 and SW7240 were retained as a plausible mediator for the SD–SW separation.

Overall, the results supported an interface-governed response on galvanised steel, such that adhesive selection shaped redistribution and post-drop development rather than changing the failure locus.

CRediT authorship contribution statement

Jakob Boretzki: Writing – review & editing, Project administration, Methodology, Investigation, Funding acquisition, Data curation, Conceptualization; **Matthias Albiez:** Writing – review & editing, Supervision, Project administration, Methodology, Investigation, Funding acquisition; **Thomas Ummenhofer:** Supervision, Resources; **Justus Mantik:** Writing – review & editing, Investigation; **Maik Dörre:** Writing – review & editing, Investigation, Funding acquisition; **Morten Voß:** Writing – review & editing; **Till Vallée:** Writing – original draft, Visualization, Supervision, Funding acquisition, Data curation; **Tobias Evers:** Writing – review & editing, Investigation.

Declaration of competing interest

The authors declare that they have no known competing financial interests or personal relationships that could have appeared to influence the work reported in this paper.

Acknowledgments

The research project *"Pretensioned hybrid connections in hot-dip galvanised steel structures subject to complex stresses"* was funded by the Federal Ministry of Economic Affairs and Energy as part of the "Industrial Collective Research" programme on the basis of a resolution of the German Bundestag. This project 01IF22360N/P 1570 from the Research Association for steel Application (FOSTA), Düsseldorf, was carried out at Karlsruhe Institute of Technology, Fraunhofer IGP and IFAM.

Data availability

Data will be made available on request.

References

[1] T. Vallée, M. Albiez, 17 - building and construction steel and aluminium, in: R.D. Adams (Ed.), Adhesive Bonding (Second Edition), Woodhead Publishing, 2021, pp. 525–569. https://doi.org/10.1016/B978-0-12-819954-1.00019-8.

[2] T. Ummenhofer, J. Boretzki, M. Albiez, Hybrid connection technologies for hollow sections in steel construction, Steel Constr. 15 (1) (2022) 55–72. https://doi.org/10.1002/stco.202100048.

[3] H. Pasternak, A. Schwarzlos, N. Schimmack, The application of adhesives to connect steel members, J. Constr. Steel Res. 60 (5) (2004) 649–658. https://doi.org/10.1016/S0143-974X(03)00134-2.

[4] C. Denkert, T. Gerke, R. Glienke, M. Dörre, M.K. Henkel, H. Fricke, S. Myslicki, M. Kaufmann, M. Voß, T. Vallée, Experimental investigations on pre-tensioned hybrid joints for structural steel applications, J. Adhes. 99 (2) (2023) 117–152. https://doi.org/10.1080/00218464.2021.2003786.

[5] L. Bouazaoui, A. Li, J.M. Michel, H. Hamelin, Experimentation and analytical approach of the behaviour of bonded steel-concrete composite beams, J. Constr. Steel Res. 63 (9) (2007) 1268–1278. https://doi.org/10.1016/j.jcsr.2006.11.002.

[6] B. Abeln, T. Pinger, C. Richter, M. Feldmann, Adhesion of batch hot-dip galvanized components, Int. J. Adv. Manuf. Technol. 125 (11) (2023) 5197–5209. https://doi.org/10.1007/s00170-023-11045-5.

[7] K. Sullivan, K.D. Peterman, A review of adhesive steel-to-steel connections for use in heavy construction, J. Constr. Steel Res. 213 (2024) 108405. https://doi.org/10.1016/j.jcsr.2023.108405.

[8] R.T. Foster, K.J. Schroeder, Adhesive bonding to galvanized steel: I. Lap shear strengths and environmental durability, J. Adhes. 24 (2–4) (1987) 259–278. https://doi.org/10.1080/00218468708075432.

[9] R.T. Foister, Adhesive bonding to galvanized steel: II. Substrate chemistry, morphology and bond failure analysis, J. Adhes. 24 (2–4) (1987) 279–313. https://doi.org/10.1080/00218468708075433.

[10] S. Maeda, Surface chemistry of galvanized steel sheets relevant to adhesion performance, Prog. Org. Coat. 28 (1996) 227–238. https://doi.org/10.1016/0300-9440(95)00610-9.

[11] A. Jouan, A. Constantinescu, A critical comparison of shear tests for adhesive joints, Int. J. Adhes. Adhes. 84 (2018) 63–79. https://doi.org/10.1016/j.ijadhadh.2018.02.035.

[12] L.F. da Silva, P.J. das Neves, R. Adams, J. Spelt, Analytical models of adhesively bonded joints-Part I: literature survey, Int. J. Adhes. Adhes. 29 (3) (2009) 319–330. https://doi.org/10.1016/j.ijadhadh.2008.06.005.

[13] L.F. da Silva, P.J. das Neves, R. Adams, A. Wang, J. Spelt, Analytical models of adhesively bonded joints-Part II: comparative study, Int. J. Adhes. Adhes. 29 (3) (2009) 331–341. https://doi.org/10.1016/j.ijadhadh.2008.06.007.

[14] H. Fricke, T. Vallée, Numerical modeling of hybrid-bonded joints, J. Adhes. 92 (7–9) (2016) 652–664. https://doi.org/10.1080/00218464.2015.1100995.

[15] T. Vallée, H. Fricke, S. Myslicki, M. Kaufmann, M. Voß, C. Denkert, R. Glienke, M. Dörre, M.-K. Henkel, T. Gerke, Modelling and strength prediction of pre-tensioned hybrid bonded joints for structural steel applications, J. Adhes. 98 (11) (2022) 1573–1613, published online 24 May 2021. https://doi.org/10.1080/00218464.2021.1928498.

[16] L.F.M. da Silva, M. Pirondi, A. Öchsner (Eds.), Hybrid Adhesive Joints, Springer, Berlin, Heidelberg, 2011. https://doi.org/10.1007/978-3-642-16623-5.

[17] K. Yokozeki, K. Hisazumi, T. Vallée, T. Evers, T. Ummenhofer, J. Boretzki, M. Albiez, Hybrid joints consisting of pre-tensioned bolts and a bonded connection—Part I: local approach, Int. J. Adhes. Adhes. 132 (2024) 103713. https://doi.org/10.1016/j.ijadhadh.2024.103713.

[18] K. Yokozeki, K. Hisazumi, T. Vallée, T. Evers, T. Ummenhofer, J. Boretzki, M. Albiez, Hybrid joints consisting of pre-tensioned bolts and a bonded connection, Part II: large-scale experiments, Int. J. Adhes. Adhes. 128 (2024) 103523. https://doi.org/10.1016/j.ijadhadh.2023.103523.

[19] J. Boretzki, M. Albiez, Static strength and load bearing behaviour of hybrid bonded bolted joints: experimental and numerical investigations, J. Adhes. 99 (4) (2022) 606–631. https://doi.org/10.1080/00218464.2022.2033619.

[20] Y. Liang, F. Xu, W. Feng, Effect of hole deformation on bolt load transfer in hybrid-bonded/bolted joints, J. Constr. Steel Res. 216 (2024) 108620. https://doi.org/10.1016/j.jcsr.2024.108620.

[21] B. Beylergil, H. Ulus, M.E. Çetin, H.B. Kaybal, S. Yildirim, A. Al-Nadhari, M. Yildiz, Fracture and fatigue assessment of bonded composite patch repairs in

notched and cracked plates, Polymers 18 (8) (2026) 912. https://doi.org/10.3390/polym18080912.
[22] H. Senol, H. Ulus, C. Yildirim, A. Al-Nadhari, S. Topal, M. Yildiz, Assessing fracture toughness performance of adhesively bonded carbon fiber/epoxy composite joints accompanied by acoustic emission inspection: effect of surface treatment methods, Eng. Fract. Mech. 321 (2025) 111119. https://doi.org/10.1016/j.engfracmech.2025.111119.
[23] H. Ulus, H.B. Kaybal, H.S. Sas, A. Avci, Flush-patch aluminum–frp repair joints for construction and retrofitting: effects of laminate type, hybrid bonding and pan nanofiber interleaves under pre-damage and hygrothermal ageing, Int. J. Adhes. Adhes. 148 (2026) 104300. https://doi.org/10.1016/j.ijadhadh.2026.104300.
[24] E. Dragoni, P. Mauri, Intrinsic static strength of friction interfaces augmented with anaerobic adhesives, Int. J. Adhes. Adhes. 20 (4) (2000) 315–321. https://doi.org/10.1016/S0143-7496(99)00062-7.
[25] J.-Y. Cognard, R. Créac'hcadec, L. Sohier, P. Davies, Analysis of the nonlinear behavior of adhesives in bonded assemblies—comparison of TAST and Arcan tests, Int. J. Adhes. Adhes. 28 (8) (2008) 393–404. https://doi.org/10.1016/j.ijadhadh.2008.04.006.
[26] K. Yokozeki, T. Vallée, T. Evers, M. Albiez, J. Boretzki, T. Ummenhofer, Multiaxial stress effects on bonding strength in adhesively bonded joints, J. Adhes., Published online, (2024), https://doi.org/10.1080/00218464.2024.2338525.
[27] K. Yokozeki, T. Evers, T. Vallée, Impact of joint geometries in bonded-bolted hybrid joints for steel construction, J. Constr. Steel Res. 211 (2023) 108166. https://doi.org/10.1016/j.jcsr.2023.108166.
[28] T. Evers, P. Richter, T. Vallée, K. Yokozeki, M.A. Viehöfer, A joint effort: probabilistic methods for hybrid joint strength prediction, Int. J. Adhes. Adhes. 143 (2025) 104156. https://doi.org/10.1016/j.ijadhadh.2025.104156.
[29] T. Evers, T. Vallée, M.A. Viehöfer, T. Pinger, J. Mantik, M. Dörre, M. Albiez, J. Boretzki, Insights into failure in hybrid joints on galvanized steel, J. Adhes. 102 (3) (2026) 249–273. https://doi.org/10.1080/00218464.2025.2530652.
[30] K. Yokozeki, T. Evers, T. Vallée, Hybrid joints consisting of pre-tensioned bolts and a bonded connection — the influence of adhesives on the load-bearing capacity, Int. J. Adhes. Adhes. 132 (2024) 103689. https://doi.org/10.1016/j.ijadhadh.2024.103689.
[31] K. Yokozeki, T. Vallée, F. Mohr, T. Evers, Adhesive layer thickness in hybrid joints, J. Adhes. 100 (15) (2024) 1397–1420. https://doi.org/10.1080/00218464.2024.2313698.
[32] T. Evers, M.A. Viehöfer, M. Voß, T. Vallée, K. Yokozeki, Role of bolt pretension in determining stress and load-bearing capacity of hybrid joints, Int. J. Adhes. Adhes. 140 (2025) 103961. https://doi.org/10.1016/j.ijadhadh.2025.103961.
[33] B.L. Welch, On the comparison of several mean values: an alternative approach, Biometrika 38 (3/4) (1951) 330–336, http://www.jstor.org/stable/2332579.